ADVANCING EARTH AND SPACE SCIENCES

Geophysical Research Letters

RESEARCH LETTER
10.1029/2025GL116964

Assimilation of Ground and Satellite Magnetic Observations Unravels the Ionospheric, Magnetospheric, and Induced Fields During the May and October 2024 Geomagnetic Storms

Alexander Grayver[1], Jingtao Min[2], Nils Olsen[3], and Ashley Smith[4]

[1]Institute of Geophysics and Meteorology, University of Cologne, Cologne, Germany, [2]Institute of Geophysics, ETH Zurich, Zurich, Switzerland, [3]DTU Space, Technical University of Denmark, Kongens Lyngby, Denmark, [4]School of GeoSciences, University of Edinburgh, Edinburgh, UK

Key Points:

- Novel data assimilation method to model global magnetic field variations due to ionospheric, magnetospheric, and Earth-induced sources
- Significant local-time effects in magnetospheric sources at storm onset and during the main phase
- Strong correlation between mid-latitude ionospheric and magnetospheric magnetic fields during the storm

Supporting Information:

Supporting Information may be found in the online version of this article.

Correspondence to:

A. Grayver,
agrayver@uni-koeln.de

Citation:

Grayver, A., Min, J., Olsen, N., & Smith, A. (2025). Assimilation of ground and satellite magnetic observations unravels the ionospheric, magnetospheric, and induced fields during the May and October 2024 geomagnetic storms. *Geophysical Research Letters*, *52*, e2025GL116964. https://doi.org/10.1029/2025GL116964

Received 28 MAY 2025
Accepted 27 AUG 2025

Author Contributions:

Conceptualization: Alexander Grayver
Data curation: Alexander Grayver, Ashley Smith
Formal analysis: Alexander Grayver, Jingtao Min, Nils Olsen
Funding acquisition: Alexander Grayver, Nils Olsen
Investigation: Alexander Grayver, Jingtao Min, Nils Olsen
Methodology: Alexander Grayver, Jingtao Min
Project administration: Alexander Grayver
Resources: Alexander Grayver, Nils Olsen
Software: Alexander Grayver

Abstract The geomagnetic storms of May and October 2024 were the strongest storms of solar cycle 25, with the *Dst* index as low as −412 nT and auroras down to low latitudes. To investigate these extreme events, we developed a global magnetic field model of magnetospheric, ionospheric, and Earth-induced contributions obtained by assimilating magnetic observations. To leverage both ground observatory and multi-satellite magnetic data from the *Swarm*, CryoSat-2, GRACE-FO, and MSS-1 satellites, we used a new modeling approach to separate the magnetospheric and ionospheric sources, and to model both external and the Earth-induced fields with a 1-hr time resolution. The high spatio-temporal resolution of the model enables investigating the coupling between the mid-latitude ionospheric and magnetospheric field sources during all phases of the geomagnetic storms. The model reveals the total magnetic field disturbance at satellite and ground altitudes, providing critical input for space weather and a more accurate representation of the geomagnetic field.

Plain Language Summary Geomagnetic storms pose hazards to ground and space infrastructure, potentially leading to blackouts in ground infrastructure such as power grids and pipeline networks or malfunctioning satellite operations and communications. Two such events in May and October 2024, caused by Coronal Mass Ejections from the Sun, were the strongest geomagnetic storms in more than 20 yr. Thanks to an operating network of ground geomagnetic observatories and multiple satellites measuring Earth's magnetic field, as well as a new modeling technique developed here, we construct a global geomagnetic model for these periods, revealing how large-scale magnetic fields and associated electric currents in the ionosphere and magnetosphere change during strong geomagnetic storms. This unlocks new insights into the structure and dynamics of the ionosphere-magnetosphere system during extreme geomagnetic events and provides critical input for a trustworthy space weather hazard assessment.

1. Introduction

The two geomagnetic storms in May and October 2024 were the strongest Space Weather events of the current solar cycle 25. Numerous scientific studies have already investigated the origin and dynamics of these events using various ground and space observations (Astafyeva et al., 2025; Das et al., 2025; Fu et al., 2025; Hayakawa et al., 2025; Lawrence et al., 2025; Lazzús & Salfate, 2024; Lee et al., 2025; Nayak et al., 2025; Parker & Linares, 2024; J. Smith et al., 2024; Tulasi Ram et al., 2024; Z. Zhang et al., 2025), and documented an ample citizen science response (Grandin et al., 2024; Spogli, 2024). These two storms were observed with a constellation of highly accurate geomagnetic satellites, including ESA's *Swarm* trio (Olsen & Floberghagen, 2018; Olsen et al., 2013), the first low-inclination Macau Science Satellite MSS-1 (K. Zhang, 2023), as well as high-quality platform magnetometers onboard the GRACE-FO (Stolle et al., 2021) and CryoSat-2 (Olsen et al., 2020) satellites. Combining this multi-satellite constellation with ground geomagnetic observations provides a unique opportunity to separate and investigate the rapid global dynamics of the ionospheric and magnetospheric fields during all storm phases with an unprecedented spatio-temporal resolution.

In this study, we combine ground and multi-satellite magnetic field observations to construct a data-based hourly model of the time-varying mid-latitude ionospheric and magnetospheric fields. Existing models that combine ground and satellite observations, for example, the Comprehensive Model (Sabaka et al., 2020) or CHAOS

Validation: Alexander Grayver, Ashley Smith
Visualization: Alexander Grayver, Jingtao Min
Writing – original draft: Alexander Grayver
Writing – review & editing: Alexander Grayver, Jingtao Min, Nils Olsen, Ashley Smith

(Finlay et al., 2020) model series, are typically limited to night-side data and/or magnetic quiet times because their primary goal is to constrain the time-varying core field. Dedicated ionospheric magnetic field models (e.g., Chulliat et al. (2016) and Yamazaki (2022)) use *Swarm* satellite data to infer ionospheric currents during magnetic quiet times. Recent studies also combined the output of the physical ionospheric dynamics model TIE-GCM with observed time-varying magnetic fields (Egbert et al., 2020; Zenhäusern et al., 2021). However, these approaches used only ground observations and, as such, cannot separate ionospheric and magnetospheric sources since both are external sources for an observer at the Earth's surface. Another characteristic of these models is a prescribed (explicitly or implicitly) temporal behavior, mostly restricting the model to a set of solar, lunar, and seasonal harmonics, which sometimes are further modulated by a proxy variable such as the F10.7 solar flux to mimic solar activity levels. While these models accurately describe mid-latitude ionospheric currents during quiet times and also account for some magnetospheric field components (Maus & Lühr, 2005), the periodic basis functions used in these models are not suited for describing the rapid non-periodic variations occurring during geomagnetic storms.

Further, many geomagnetic field models do not account for 3-D induction effects due to the heterogeneous conductivity of the solid Earth and oceans (Kuvshinov, 2008). Induced fields affect both the amplitude and phase of the observed magnetic field. In addition, induction effects differ between ground and satellite observations due to the scale-dependent attenuation (Grayver et al., 2021). Therefore, a proper modeling of 3-D induction effects is needed in order to quantitatively study the ionospheric sources using ground and satellite magnetic field observations. Presently, only a few studies have attempted to account for induction effects; however, they only model induction effects at a few diurnal harmonics due to ionospheric sources (Chulliat et al., 2016; Sabaka et al., 2002) or only account for the dominant induction effect due to magnetospheric sources (Finlay et al., 2020).

To enable the study of ionospheric and magnetospheric sources during all magnetic conditions and local times, Min and Grayver (2025) developed a technique to separate ionospheric, magnetospheric, and induced magnetic field sources using both ground and multi-satellite observations. Using this approach, the authors constructed a time-varying Spherical Harmonic (SH) model of the ionospheric and magnetospheric sources for 2014–2023 with a time resolution of 3 hr. The methodology employed in the present study is similar to Min and Grayver (2025), but with several notable further developments. First, instead of co-estimating a low-degree model of internal induced fields, we developed a new approach that allows us to consistently co-model the electromagnetic (EM) induction response of the 3-D solid Earth and oceans. We achieve this by fitting the data to a set of basis functions that satisfy Maxwell's equations governing magnetic field behavior in and outside a spherical Earth with a prescribed electrical conductivity structure. Second, in addition to *Swarm* observations and platform magnetometer data from CryoSat-2 and GRACE-FO, we include data from the low-inclination MSS-1 satellite, leading to a higher spatio-temporal resolution of the model. We apply this approach to construct the first hourly model of mid-latitude ionospheric and magnetospheric currents for the severe geomagnetic storms of May and October 2024.

2. Methods

The magnetic field vector $\vec{B}$ at a location $\vec{r}$ and time t is described by Maxwell's equations under the quasi-static approximation

$$\nabla \times \vec{E}(\vec{r},t) = -\frac{\partial \vec{B}(\vec{r},t)}{\partial t}, \tag{1}$$

$$\nabla \times \vec{B}(\vec{r},t) = \mu\left[\sigma(\vec{r})\,\vec{E}(\vec{r},t) + \vec{j}^{\,\text{ext}}(\vec{r},t)\right], \tag{2}$$

$$\nabla \cdot \vec{B}(\vec{r},t) = 0, \tag{3}$$

where $\vec{r} = (r,\theta,\phi)$ is the position vector in the geocentric spherical frame, σ is the electrical conductivity of the solid Earth and oceans. We assume $\mu \equiv \mu_0$, that is the magnetic permeability of free space throughout the model domain. The vectors $\vec{B}, \vec{E}$ and $\vec{j}$ denote the magnetic field, electric field, and the current density, respectively.

In addition to the solenoidal condition (Equation 3), the magnetic field is assumed to be irrotational (i.e., $\nabla \times \vec{B} = 0$) at the observation points. This assumption implies that the magnetic field is a Laplacian potential field and that observations are conducted in regions with no electric currents, separated from those carrying ionospheric and magnetospheric currents. Further, we define the term $\vec{j}^{\,\mathrm{ext}}$ as the current density in a thin shell at an altitude h above the Earth's reference radius a, thus

$$\vec{j}^{\,\mathrm{ext}}(\vec{r},\omega) = -\delta(r-(a+h))\hat{e}_r \times \nabla_H \Psi(\theta,\phi,t), \quad (4)$$

where ∇_H is surface gradient and $\hat{e}_r$ is the unit vector in radial direction. Such a current sheet at an altitude h can be used to model the magnetic field above or below due to the stream function Ψ. The stream function Ψ can be expanded using arbitrary functions such as current loops, spherical elementary currents, dipoles, spherical harmonics, or a combination thereof. Since we aim to construct a global model, we chose to work with complex SH functions $S_n^m(\theta,\phi) = P_n^{|m|}(\cos\theta)\exp(im\phi)$, with n, m denoting degree n and order m, and $P_n^{|m|}$ being Schmidt semi-normalized associated Legendre functions. Specifically, we parameterize equivalent currents due to external sources in the ionospheric E-layer by using $h = 110$ km and

$$\Psi(\theta,\phi,t) = -\frac{a}{\mu_0}\sum_{n,m}\frac{2n+1}{n+1}\left(\frac{a+h}{a}\right)^n \varepsilon_{nm}^{\mathrm{ion}}(t) S_n^m(\theta,\phi), \quad (5)$$

where $\varepsilon_{nm}^{\mathrm{ion}}(t)$ are the corresponding ionospheric SH coefficients and $\sum_{n,m} = \sum_{n=1}^{\infty}\sum_{m=-n}^{m=n}$. Equation 5 is a valid representation of the potential poloidal field in the region $a \le r < (a+h)$ due to external sources described by $\varepsilon_{nm}^{\mathrm{ion}}(t)$. For region $r > (a+h)$ where satellites fly, an equivalent stream function for ionospheric sources of internal origin can be written as

$$\Psi(\theta,\phi,t) = \frac{a}{\mu_0}\sum_{n,m}\frac{2n+1}{n}\left(\frac{a}{a+h}\right)^{n+1} \iota_{nm}^{\mathrm{ion}}(t) S_n^m(\theta,\phi), \quad (6)$$

where $\iota_{nm}^{\mathrm{ion}} = -\frac{n}{n+1}\left(\frac{a+h}{a}\right)^{2n+1}\varepsilon_{nm}^{\mathrm{ion}}$ (Sabaka et al., 2010; Schmucker, 1985).

The magnetospheric currents are assumed to be external to both satellites and ground observatories. Therefore, we parameterize them via external SH coefficients $\varepsilon_{nm}^{\mathrm{mag}}(t)$. Since magnetospheric sources are of external origin, there is no need to introduce an equivalent current formulation. However, we note that using $\varepsilon_{nm}^{\mathrm{mag}}$ instead of $\varepsilon_{nm}^{\mathrm{ion}}$ in Equation 5 reproduces the external field due to $\varepsilon_{nm}^{\mathrm{mag}}$ in the region $a \le r < (a+h)$ exactly. Parameterizing the ionospheric current as a sheet current and assuming that the observed magnetic field is a Laplacian potential field allows for a unique determination and separation of the ionospheric and magnetospheric magnetic field by joint analysis of ground and satellite observations (Min & Grayver, 2025; Sabaka et al., 2010).

Electric currents induced in the oceans and solid Earth remain internal to both satellites and ground observations. Instead of parameterizing the internal induced field by using additional unknown variables (i.e., by introducing a separate set of SH coefficients), we co-model the induced field as explained below. Specifically, we follow Min and Grayver (2025) (their Equations 13 and 14) and expand the magnetic field in terms of magnetospheric, ionospheric, and induced parts. Subsequently, the induced part is replaced with the induction kernels following the methodology in Grayver et al. (2021). This approach yields magnetic field basis functions $\hat{B}_{nm}^{\mathrm{ion}}, \hat{B}_{nm}^{\mathrm{mag}}$ describing ionospheric (respectively magnetospheric) magnetic field contributions plus their Earth-induced counterparts for a given coefficient $\varepsilon_{nm}^{\mathrm{ion}}$ or $\varepsilon_{nm}^{\mathrm{mag}}$. These basis functions satisfy Equations 1 and 2 for an extraneous current density Equation 4 given by individual SH modes and unit coefficients. Thus, they can be used to represent the magnetic field due to an arbitrary current density distribution at time t as

$$\vec{B}^{\mathrm{mod}}(\vec{r},t;\sigma,\mathbf{m}) = \sum_{n,m}\int_{-\infty}^{t}\left[\hat{B}_{nm}^{\mathrm{ion}}(\vec{r},t-\tau;\sigma)\varepsilon_{nm}^{\mathrm{ion}}(\tau) + \hat{B}_{nm}^{\mathrm{mag}}(\vec{r},t-\tau;\sigma)\varepsilon_{nm}^{\mathrm{mag}}(\tau)\right]\mathrm{d}\tau, \quad (7)$$

where $\mathbf{m}(t) = \{\varepsilon_{nm}^{\text{ion}}(t), \varepsilon_{nm}^{\text{mag}}(t)\}$ is a vector function of time containing SH coefficients describing ionospheric and magnetospheric sources. Note that due to a finite conductivity of the solid Earth and oceans, the field depends on both the instantaneous and the past values of the ionospheric and magnetospheric currents, hence the convolution integral in Equation 7. Although its lower limit extends to infinity, we set the lower limit to 4 months (or the maximum available time if it is shorter than 4 months) in practice, which ensures that the quantities $\hat{B}_{nm}^{\text{ion}}, \hat{B}_{nm}^{\text{mag}}$ have decayed sufficiently and that the majority of the transient Earth's response has been accounted for (Grayver et al., 2021). Finally, SH coefficients describing the ionospheric and magnetospheric fields are estimated by solving a minimization problem

$$\min_{\mathbf{m}} \int_{t_0}^{t_1} \int_{D} L\left[\vec{B}^{\text{obs}}(\vec{r}, t) - \vec{B}^{\text{mod}}(\vec{r}, t; \sigma, \mathbf{m})\right] \mathrm{d}\mathcal{D}\mathrm{d}t, \tag{8}$$

where $L[\cdot]$ is the Huber loss function that is robust to outliers and large residuals (Owen, 2007). The data loss is then integrated over observations $\mathcal{D}$ and the assimilated time interval $[t_0, t_1]$.

A key difference of Equation 8 from a conventional Gauss separation approach is that the basis functions $\hat{B}_{nm}^{\text{ion}}, \hat{B}_{nm}^{\text{mag}}$ from Equation 7 satisfy the governing equations Equations 1 and 2 for a given electric conductivity model of the Earth and oceans, thereby consistently accounting for the EM induction effects in these layers. The additional advantage is that once Equation 8 is solved, the magnetic field $\vec{B}$ that best explains observations and obeys governing equations can be easily calculated everywhere outside the source region, enabling a detailed analysis of both inducing currents and associated primary and induced electromagnetic fields. The corresponding electric field $\vec{E}$ is also readily accessible and can be useful for the characterization of GICs, but this topic is beyond the scope of this paper.

In practice, we split the interval $[t_0, t_1]$ into non-overlapping discrete time bins. Ionospheric and magnetospheric coefficients $\varepsilon_{nm}^{\text{ion}}, \varepsilon_{nm}^{\text{mag}}$ are assumed to be constant in each time bin. Therefore, the integral in Equation 8 becomes a sum over discrete time bins and the available observational points, whereby SH coefficients are estimated for each time bin by minimizing the Huber loss function $L[\cdot]$ over a subset of observations that fall into the bin. We used the implementation of the Huber regression (Owen, 2007) provided by the *scikit-learn* software package (Pedregosa et al., 2011). With the current data distribution, we chose to work with 1-hr bins and estimate coefficients up to SH degree and order three.

The methodology to evaluate Equation 7 in discrete time bins has been elaborated in detail in Grayver et al. (2021) and Kruglyakov et al. (2022). This methodology involves calculating a representation of functions $\hat{B}_{nm}^{\text{ion}}, \hat{B}_{nm}^{\text{mag}}$ in finite time bins, which involves the numerical solution of Equations 1 and 2 using the finite element induction solver (Grayver & Kolev, 2015; Grayver et al., 2019) for an a priori Earth's conductivity model. The conductivity model σ used here consists of the 1-D mantle conductivity profile from Grayver et al. (2017) overlain by the 3-D ocean and sediments model of Grayver (2021).

3. Data

We use geomagnetic data between January and November 2024. Observations from all three ESA *Swarm* satellites (Olsen et al., 2013) and MSS-1 (Jiang et al., 2024; K. Zhang, 2023) were used, complemented by the platform magnetometer data from the CryoSat-2 (Olsen et al., 2020) and GRACE-FO (Stolle et al., 2021) spacecrafts, all downsampled to 1-min values. For ground observatory data, we used hourly mean values from the *AUX_OBS* product (Macmillan & Olsen, 2013) that delivers (quasi-)definitive data from INTERMAGNET and the World Data Centre for Geomagnetism. We used only the horizontal components in ground observatory data since they are much less affected by the poorly constrained 3-D subsurface induction effects compared to the vertical component (Grayver, 2021; Kuvshinov, 2008; Olsen & Kuvshinov, 2004). Except for the MSS-1 data, all other observations were retrieved using the *VirES for Swarm* Python client (A. Smith et al., 2025). The core and crustal field values as given by the CHAOS-8 model (Kloss et al., 2025) were subtracted from the data. The remaining biases in the observatory data were accounted for following the approach of Min and Grayver (2025). Data poleward of ±55° quasi-dipole latitude were excluded to avoid the effects of small-scale polar current systems, which require dedicated approaches to be modeled accurately.

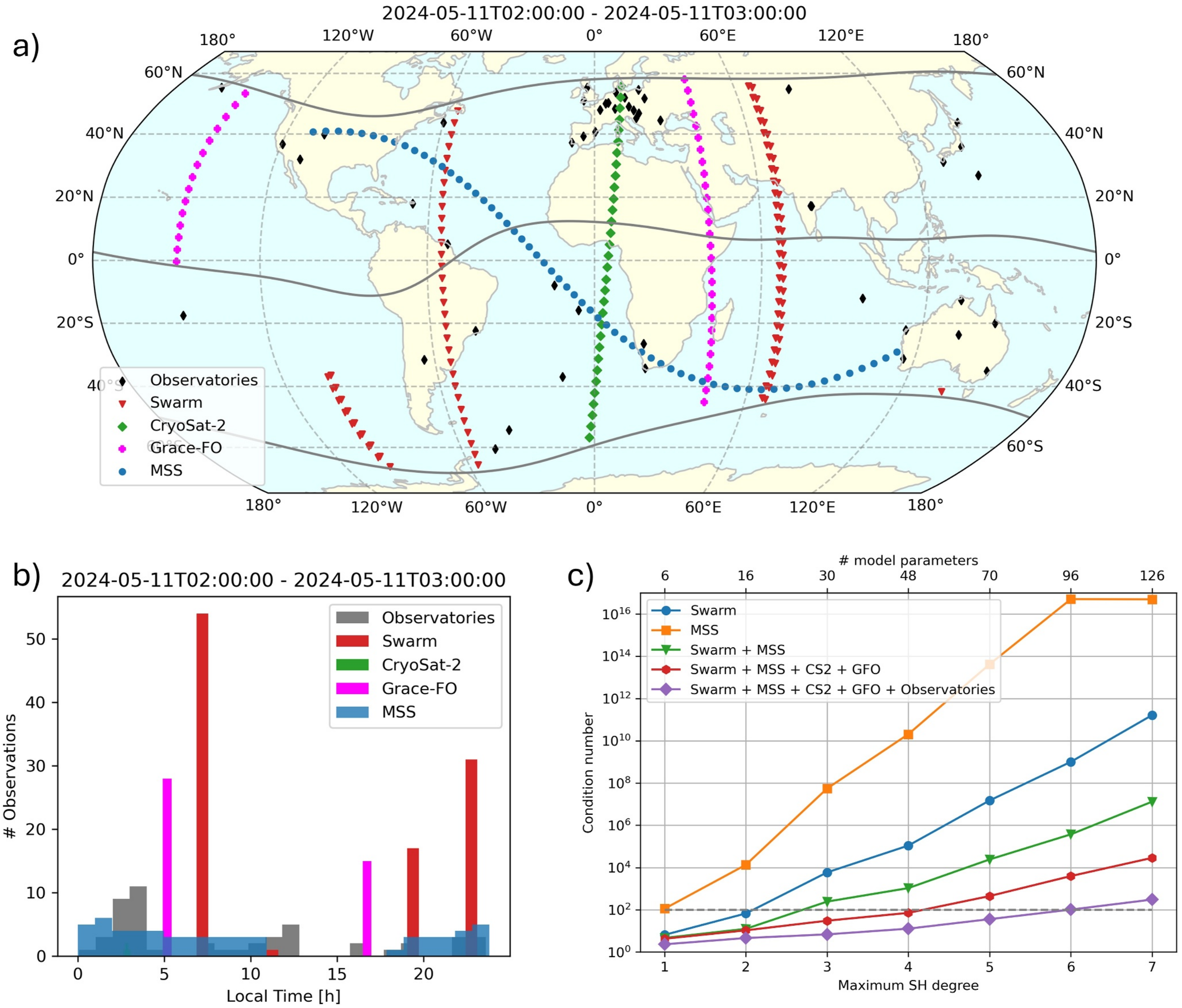

Figure 1. (a) Distribution of used space and ground data for 1 hr time window. Gray lines depict the dip equator and ±55° QD latitudes. Satellite data was decimated to 1 min. (b) Number of observations for each local time. Each observation is a 3-component vector field, $\vec{B}(\vec{r}, t)$, at a given time and location. (c) Condition number of the forward operator as a function of the maximum degree for different combinations of satellite and observatory data. The dashed line shows a threshold of 100.

Figures 1a and 1b show the geographic and local time coverage of the data for a single hourly time window around the May 2024 storm peak. Figure 1c shows the condition number of the forward operator for the same time window and varying maximum degree of the SH expansion for different combinations of data. Large condition numbers imply high co-linearity (linear dependency) between different SH coefficients, resulting in poor separation of coefficients and significant amplification of noise (Hansen, 1998). Combining ground and satellite data yields the lowest condition number and allows for a higher spatial resolution. Notably, since the induced fields are co-modeled, the separation of ionospheric and magnetospheric coefficients is, in principle, possible with satellite data alone, as evidenced by the finite condition numbers for models that utilize at least one polar satellite. In practice, noise (in particular in platform magnetometer data) and non-modeled sources, as well as gaps in data and insufficient local time separation, may result in significant deterioration of the model's quality (Figure S7 in Supporting Information S1). Therefore, the joint use of ground observatories and satellites is important for stabilizing the problem and ensuring that sources are separated.

10.1029/2025GL116964

Finally, note that the condition number varies in each time window as a result of differences in data distribution, primarily defined by satellite orbits and available observatories. We chose the maximum SH degree of three for both ionospheric and magnetospheric coefficients, resulting in 30 coefficients to be estimated in each time window. This yields the condition number of ≈10 for the majority of time windows (Figure S6 in Supporting Information S1), ensuring stability of the inverse problem.

4. Results

Thanks to our geomagnetic assimilation method and multi-satellite observations, we can reliably separate the magnetic fields of ionospheric and magnetospheric origins in hourly bins. Figure 2 shows the time series of ionospheric and magnetospheric SH coefficients during the May and October 2024 storms. The real SH coefficients q_n^m and s_n^m shown are coefficients for the cosine and sine components of the real spherical harmonics, respectively. These are related to complex coefficients ε_{nm} as

$$q_n^0 = \varepsilon_{n0}, \qquad \begin{cases} q_n^m = 2\mathrm{Re}[\varepsilon_{nm}] \\ s_n^m = -2\mathrm{Im}[\varepsilon_{nm}], \end{cases} \quad m > 0. \tag{9}$$

These are shown together with the coefficient of determination R^2, defined for every hour as

$$R^2 = 1 - \frac{\|\mathbf{B}^{\mathrm{obs}} - \mathbf{B}^{\mathrm{mod}}\|_2^2}{\|\mathbf{B}^{\mathrm{obs}}\|_2^2 - N_d \overline{\mathbf{B}^{\mathrm{obs}}}^2}, \tag{10}$$

where $\mathbf{B} \in \mathbb{R}^{N_d \times 1}$ is a vector that contains the observed or predicted magnetic fields and $\overline{\mathbf{B}}$ is the arithmetic mean. These vectors include all three magnetic components for satellite data and the two horizontal components for ground observatory data.

The R^2 statistics in Figure 2 shows that our model explains more data variance during the recovery phases of the storm, where most of the variance can be attributed to the large-scale magnetospheric contribution i.e. well described by low-degree spherical harmonics. Magnetospheric sources dominate during the main phase, but the ionosphere is also substantially disturbed, especially during the first 24 hr after the storm onset, with all ionospheric coefficients showing highly dynamic non-periodic behavior. During quiet times, ionospheric zonal harmonics ($m = 0$) are negligible while local time terms (e.g., P_2^1, P_3^2) are the strongest. During the storm's main phase, zonal harmonics in the ionosphere exhibit significant magnitude, indicating the existence of ionospheric sources at all local times. It takes around 36 hr after the storm peak for the periodic quiet-time Sq pattern and corresponding diurnal harmonics to recover, as is well visible in the SH coefficients representing local time terms. In addition to Sq current system, some of the observed mid-latitude variability is likely due to the penetration electric field and disturbance dynamo electric field (Fejer et al., 2016; Yamazaki & Maute, 2017) that affect mid-latitude electric currents and their respective geomagnetic signatures.

The upper part of Figure 3 shows correlation matrices between coefficients during quiet and storm times in May and October 2024. During quiet times, correlations remain low between all pairs of coefficients except for the P_2^1 coefficients. The higher correlation between the P_2^1 coefficients during quiet times is likely explained by the fact that both exhibit diurnal periodicity in the Earth-fixed frame, related to the Sq current system in the ionosphere and the combined effect of quiet-time tail and magnetopause currents (Maus & Lühr, 2005). However, around the storm peaks, all coefficients show significant (absolute value >0.5) correlations. Notably, the strongest correlation is most often between SH modes of the same degree and order. To further explore this correlation, the scatter plots for selected coefficients are shown at the bottom of Figure 3 (Figure S3 in Supporting Information S1 shows scatter plots for all coefficients). Colored by the corresponding *Dst* index, these plots further confirm the weak (respectively strong) correlation between magnetospheric and ionospheric coefficients for quiet (respectively disturbed) times, suggesting a coupling between the mid-latitude magnetosphere and ionosphere during global geomagnetic storms.

Ionospheric and magnetospheric stream functions and equivalent thin sheet currents are visualized in Figure 4. To facilitate comparison, both ionospheric and magnetospheric stream functions were calculated at 110 km altitude.

10.1029/2025GL116964

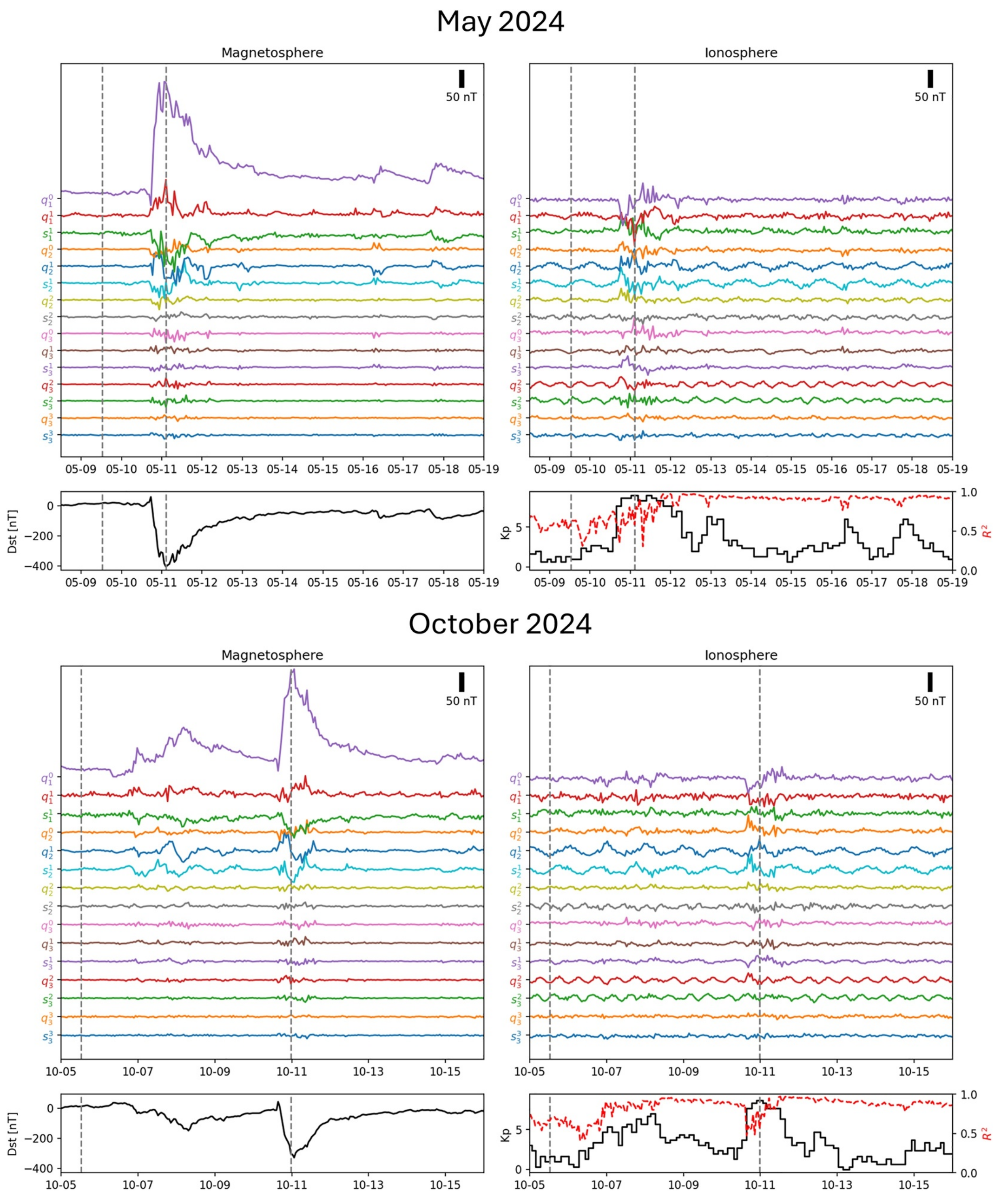

Figure 2. Time series of magnetospheric (left) and ionospheric (right) Spherical Harmonic coefficients for 10-day periods during the May and October 2024 geomagnetic storms, determined by assimilating ground and multi-satellite magnetic fields. The vertical baseline offset between adjacent time series is 50 nT. Bottom plots show *Dst* and Kp indices together with the R^2 statistics of the model (red dashed line). Vertical dashed lines denote time instances plotted in Figures 4 and 5.

We note that this is done purely for comparison; the actual magnetospheric currents are external to both ground and satellite observations, and hence can not be approximated by thin-sheet currents at this altitude. The magnetospheric contribution is dominated by low-degree SH coefficients, representing the combined effect of the (partial) ring, tail, and magnetopause currents, among others (Ganushkina et al., 2018). However, as is evident from Figure 2, non-dipole ($n > 1$) and non-zonal ($m > 0$) harmonics contribute up to ≈25% to the total variance, indicating a significant non-axisymmetric structure. Among others, large non-dipolar SH coefficients suggest local time effects in magnetospheric currents that are apparent around the peaks of the May and October 2024 storms, possibly caused by partial ring or magnetotail currents. Notably, the magnitude of the magnetospheric

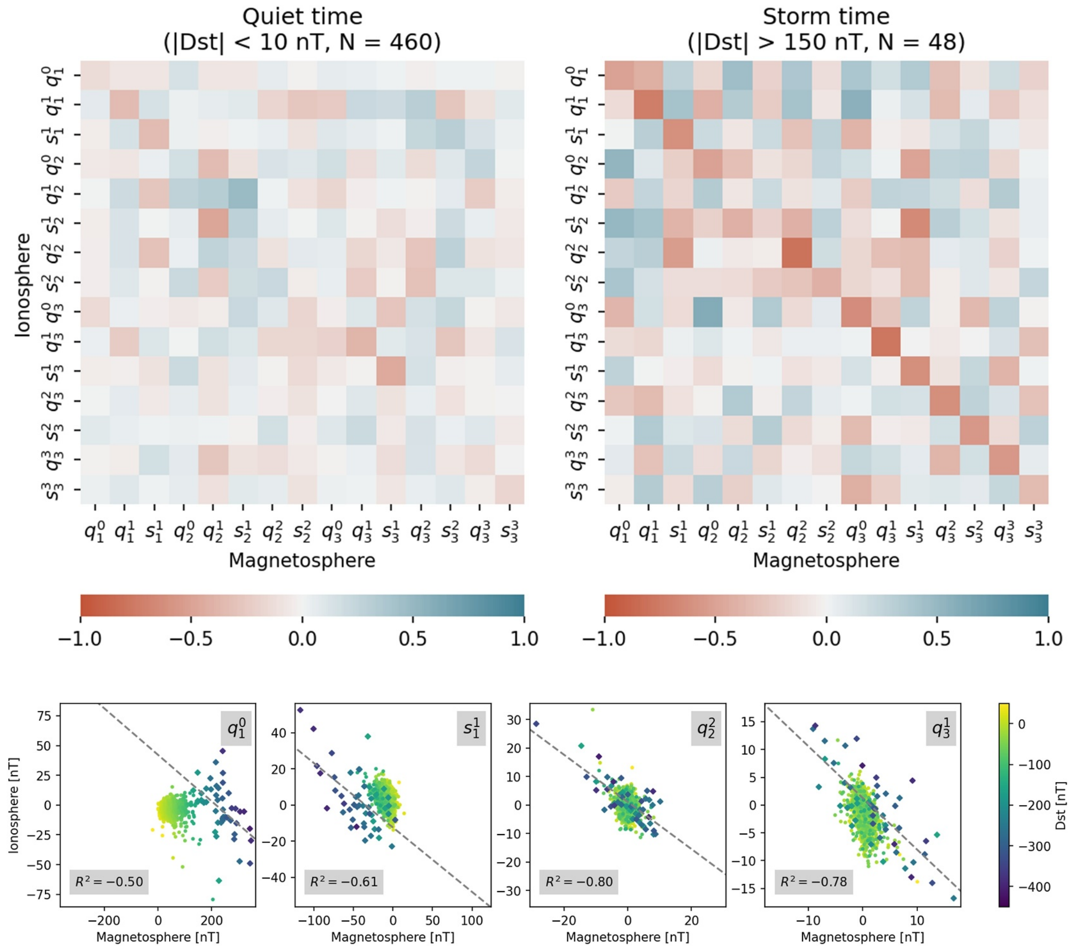

Figure 3. Top: Correlation matrix between magnetospheric and ionospheric coefficients. Bottom: Scatter plots between selected magnetospheric and ionospheric Spherical Harmonic coefficients from Figure 2. Points are colored by the corresponding *Dst* index, with diamonds used for time windows when $|Dst| > 150$ nT and circles for the rest. The linear regression lines with the R^2 statistics were calculated for each coefficient using points with $|Dst| > 150$ nT.

equivalent current is approximately an order of magnitude higher during the storm, which can be explained by a combination of the increased current density (Ganushkina et al., 2018) and the compressed magnetopause (Fu et al., 2025). The ionosphere exhibits a clear two-vortex structure characteristic of the Sq current system (Yamazaki & Maute, 2017) during quiet time, whereas much stronger and spatially complex currents are observed around the storm peak time.

The corresponding total (i.e., external plus induced) ground magnetic fields are shown in Figure 5. Both components are dominated by signatures of the Sq current system on the day side during quiet conditions. During the storm, the field is dominated by large-scale magnetospheric currents. In addition, the radial (vertical) component exhibits strong 3-D induction effects caused by the conductivity contrasts between the ocean and continents. The animated stream functions and total ground magnetic fields for the whole duration of the magnetic storms are supplemented to the paper.

5. Discussion and Conclusions

This study presents a novel approach for assimilating ground and multi-satellite geomagnetic field observations to investigate the spatio-temporal evolution of mid-latitude geomagnetic field variations caused by ionospheric and magnetospheric sources. The method uses basis functions that satisfy the electromagnetic induction equations, providing a versatile physics-based basis for assimilating ground and satellite magnetic observations, which enables co-modeling of EM fields induced in the oceans and solid Earth using an a priori model of their electrical

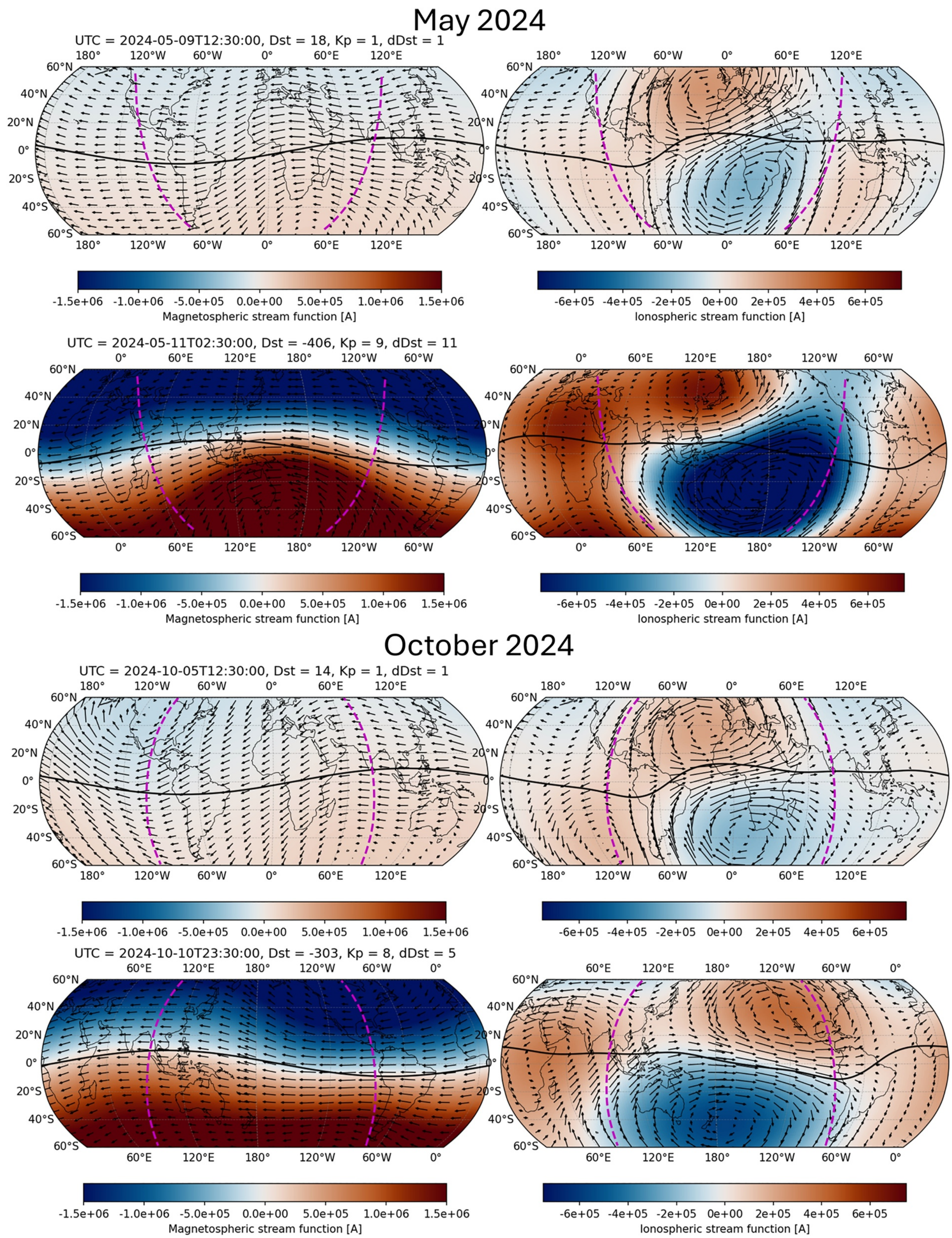

Figure 4. Magnetospheric (left) and ionospheric (right) stream functions and corresponding equivalent currents (arrows) calculated at the altitude of 110 km for two time instances, representing quiet and storm conditions. The plots are centered at local noon with dashed lines depicting dawn and dusk terminators. Solid lines correspond to the geomagnetic and quasi-dipole equator for magnetospheric and ionospheric stream functions, respectively. Note the different color scales between ionospheric and magnetospheric stream functions.

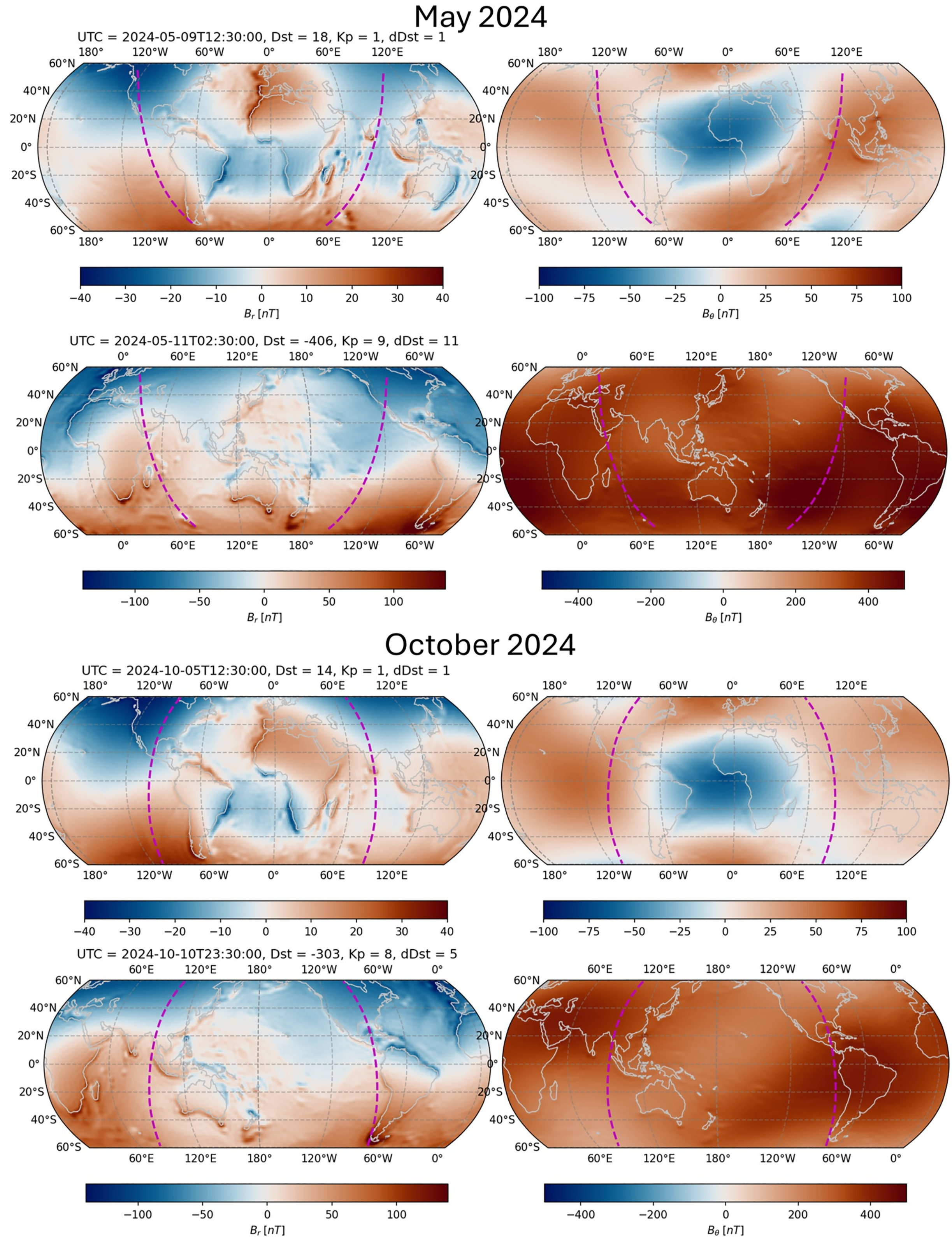

Figure 5. Radial (B_r) and southward (B_θ) components of the total magnetic field at the Earth's surface for the two time instances, corresponding to quiet and disturbed conditions (dashed lines in Figure 2). The plots are centered at local noon with dashed lines depicting dawn and dusk terminators. Note the different color scales between the plots.

10.1029/2025GL116964

conductivity. Due to this coupling of inducing (ionospheric and magnetospheric) and induced currents, there is no need to separately estimate induced fields. This enables a higher model resolution and, more critically, allows us to separate ionospheric and magnetospheric sources during all magnetic conditions.

We applied this method to describe large-scale mid-latitude ionospheric and magnetospheric fields during the extreme geomagnetic storms of May and October 2024. Our analysis unveiled a global view of how the mid-latitude ionosphere and magnetosphere interact at temporal scales down to 1 hr during all storm phases. While the SH coefficients describing ionospheric and magnetospheric sources are only weakly correlated during quiet times, there is a strong correlation between coefficients describing ionospheric and magnetospheric fields during the main and recovery phases of the storm. This provides observational evidence for coupling and energy exchange mechanisms also at mid-latitudes, potentially related to geomagnetic signatures of high-latitude currents (Aakjaer et al., 2016), penetration electric field, the onset of a disturbed ionospheric dynamo (Fejer et al., 2016; Yamazaki & Maute, 2017), or electromagnetic induction effects (Laundal et al., 2025). We found that magnetospheric equivalent currents are more than an order of magnitude stronger during the main phase of the storm, possibly resulting from a higher current density and the compressed magnetopause (Fu et al., 2025). Since our model separates magnetospheric, ionospheric, and induced sources, it allows for a more precise estimation of magnetospheric disturbances. For example, whereas the *Dst* index contains both induced and ionospheric components, the q_{10}^{mag} coefficient from our model provides an estimate of the symmetric ring current disturbance that is free of these effects, which can account for up to 30% of the *Dst* index magnitude during storms (see Figure S8 in Supporting Information S1). Therefore, our model can replace the *Dst* for example, in models based on the Dessler–Parker–Sckopke (DPS) relation (Roelof & Williams, 1988), yielding a more accurate estimation of the storm-time ring current energy.

During periods of high activity, large-scale F-region dynamo currents intensify (Alken et al., 2016; Maute & Richmond, 2016), and the field-aligned currents can propagate further equatorward, reaching even mid-latitudes (Wang et al., 2006). As a result, in situ currents at LEO satellite altitudes may significantly contribute to the observed magnetic field. To ensure that our model remains robust and the observed correlation patterns reliable, we repeated the analysis using only data at QD-latitudes $\pm(8^\circ - 45^\circ)$ (in both hemispheres), which minimizes the effect of in situ current systems developed at polar and equatorial latitudes. The resulting coefficients and correlation matrix are shown in Figures S1 and S2 in Supporting Information S1. Remarkably, the resulting coefficients are very similar to our previous ones, and the correlation between ionospheric and magnetospheric coefficients during active times is even stronger. Using the model with a stricter data selection, Figures S4 and S5 in Supporting Information S1 further show equivalent currents and ground magnetic fields for the same times as in Figures 4 and 5. The large-scale structure of both currents and the ground field is very similar between the models, confirming the robustness of the inferred behavior. However, there are still factors that potentially affect the source separation in both models. Although the model is well-conditioned and the toroidal magnetic fields produced by pure poloidal in situ F-region currents remain largely orthogonal to our forward operator (Olsen, 1997), potential in situ toroidal *F*-region currents generate a poloidal magnetic field (Sabaka et al., 2010) that is not accounted for in our model. Further, sub-hourly and fine-scale dynamics not captured by the present temporal and spatial resolution may affect the estimated model coefficients. These aspects should be pursued further in future studies.

In addition to the inferred magnetospheric and ionospheric fields described by the corresponding external SH coefficients, the approach presented here provides a physically consistent representation of electromagnetic fields outside the source regions. Besides the magnetic field disturbances calculated here (Figure 5), we are also able to compute the ground induced electric fields, accounting for 3-D subsurface conductivity variations, thus providing relevant information for space weather hazard models (Kelbert, 2020) and Geomagnetically Induced Currents predictions.

Our approach and the resulting model are formulated in geographic coordinates and removes the restriction of considering only periodic variations and/or quiet conditions, allowing for modeling broadband induction effects due to both ionospheric and magnetospheric sources. However, this limits the spatial resolution of the model since sufficient data coverage is required for each time bin. Incorporating additional observations, for example, from upcoming satellite missions such as ESA NanoMagSat (Hulot et al., 2021) or existing large constellations (Anderson et al., 2021), and maintaining the current constellation of magnetic missions will enhance the model resolution and allows us to extend the model, for instance, by modeling in situ *F*-region currents.

Data Availability Statement

ESA Swarm, CryoSat-2, GRACE-FO, and ground observations were retrieved using the Python interface to the VirES service (A. Smith et al., 2025). MSS-1 vector field magnetometer data were obtained from K. Zhang (2025). CHAOS magnetic field model was retrieved from Kloss et al. (2025). The models presented in this study can be retrieved from Grayver (2025).

Acknowledgments
AG and NO acknowledge the support from the ESA Swarm DISC Project 4000109587. AG was supported by the Heisenberg Grant from the German Research Foundation, Deutsche Forschungsgemeinschaft (Project 465486300). JM is grateful for support from the Swiss National Science Foundation Project 219247. We thank three anonymous reviewers for their insightful and constructive comments. Open Access funding enabled and organized by Projekt DEAL.

References

Aakjaer, C. D., Olsen, N., & Finlay, C. C. (2016). Determining polar ionospheric electrojet currents from swarm satellite constellation magnetic data. *Earth Planets and Space*, *68*(1), 140. https://doi.org/10.1186/s40623-016-0509-y

Alken, P., Maute, A., & Richmond, A. D. (2016). The F-region gravity and pressure gradient current systems: A review. *Space Science Reviews*, *206*(1–4), 451–469. https://doi.org/10.1007/s11214-016-0266-z

Anderson, B. J., Angappan, R., Barik, A., Vines, S. K., Stanley, S., Bernasconi, P. N., et al. (2021). Iridium communications satellite constellation data for study of Earth's magnetic field. *Geochemistry, Geophysics, Geosystems*, *22*(8), e2020GC009515. https://doi.org/10.1002/essoar.10506892.1

Astafyeva, E., Maletckii, B., Förster, M., Ouar, I. D., Huba, J. D., Hairston, M. R., & Coley, W. R. (2025). Electrodynamic and ionospheric puzzles of the 10–11 May 2024 geomagnetic superstorm. *Journal of Geophysical Research: Space Physics*, *130*(5), e2024JA033284. https://doi.org/10.1029/2024ja033284

Chulliat, A., Vigneron, P., & Hulot, G. (2016). First results from the swarm dedicated ionospheric field inversion chain. *Earth Planets and Space*, *68*(1), 1–18. https://doi.org/10.1186/s40623-016-0481-6

Das, S. K., Stolle, C., Yamazaki, Y., Rodríguez-Zuluaga, J., Wan, X., Kervalishvili, G., et al. (2025). On the F-region ionospheric plasma density distribution and irregularities response during the May-2024 geomagnetic storm observed by LEO satellites. *Geophysical Research Letters*, *52*(10), e2025GL115780. https://doi.org/10.1029/2025GL115780

Egbert, G. D., Alken, P., Maute, A., Zhang, H., & Richmond, A. (2020). Modeling diurnal variation magnetic fields for mantle induction studies. *Geophysical Journal International*, *225*(2), 1086–1109. https://doi.org/10.1093/gji/ggaa533

Fejer, B. G., Blanc, M., & Richmond, A. D. (2016). Post-storm middle and low-latitude ionospheric electric fields effects. *Space Science Reviews*, *206*(1–4), 407–429. https://doi.org/10.1007/s11214-016-0320-x

Finlay, C. C., Kloss, C., Olsen, N., Hammer, M. D., Tøffner-Clausen, L., Grayver, A., & Kuvshinov, A. (2020). The CHAOS-7 geomagnetic field model and observed changes in the South Atlantic anomaly. *Earth Planets and Space*, *72*(1), 1–31. https://doi.org/10.1186/s40623-020-01252-9

Fu, W., Fu, H., Zhang, W., Yu, Y., & Cao, J. (2025). Compression of Earth's magnetopause down to 5 R_E during the superstorm on 10 May 2024. *Geophysical Research Letters*, *52*(5), e2024GL114040. https://doi.org/10.1029/2024gl114040

Ganushkina, N. Y., Liemohn, M., & Dubyagin, S. (2018). Current systems in the Earth's magnetosphere. *Reviews of Geophysics*, *56*(2), 309–332. https://doi.org/10.1002/2017rg000590

Grandin, M., Bruus, E., Ledvina, V. E., Partamies, N., Barthelemy, M., Martinis, C., et al. (2024). The geomagnetic superstorm of 10 May 2024: Citizen science observations. *EGUsphere*, *2024*, 1–32. https://doi.org/10.5194/egusphere-2024-2174

Grayver, A. (2021). Global 3-d electrical conductivity model of the world ocean and marine sediments. *Geochemistry, Geophysics, Geosystems*, *22*(9), e2021GC009950. https://doi.org/10.1029/2021gc009950

Grayver, A. (2025). Assimilation of ground and satellite magnetic observations unravels the ionospheric, magnetospheric, and induced fields during the May and October 2024 geomagnetic storms [Dataset]. *Zenodo*. https://doi.org/10.5281/zenodo.15846277

Grayver, A., & Kolev, T. (2015). Large-scale 3D geoelectromagnetic modeling using parallel adaptive high-order finite element method. *Geophysics*, *80*(6), E277–E291. https://doi.org/10.1190/geo2015-0013.1

Grayver, A., Kuvshinov, A., & Werthmüller, D. (2021). Time-domain modeling of three-dimensional Earth's and planetary electromagnetic induction effect in ground and satellite observations. *Journal of Geophysical Research: Space Physics*, *126*(3), e2020JA028672. https://doi.org/10.1029/2020ja028672

Grayver, A., Munch, F. D., Kuvshinov, A. V., Khan, A., Sabaka, T. J., & Tøffner-Clausen, L. (2017). Joint inversion of satellite-detected tidal and magnetospheric signals constrains electrical conductivity and water content of the upper mantle and transition zone. *Geophysical Research Letters*, *44*(12), 6074–6081. https://doi.org/10.1002/2017gl073446

Grayver, A., van Driel, M., & Kuvshinov, A. V. (2019). Three-dimensional magnetotelluric modelling in spherical Earth. *Geophysical Journal International*, *217*(1), 532–557. https://doi.org/10.1093/gji/ggz030

Hansen, P. C. (1998). *Rank-deficient and discrete ill-posed problems: Numerical aspects of linear inversion*. SIAM.

Hayakawa, H., Ebihara, Y., Mishev, A., Koldobskiy, S., Kusano, K., Bechet, S., et al. (2025). The solar and geomagnetic storms in 2024 May: A flash data report. *The Astrophysical Journal*, *979*(1), 49. https://doi.org/10.3847/1538-4357/ad9335

Hulot, G., Leger, J.-M., Clausen, L. B. N., Deconinck, F., Coïsson, P., Vigneron, P., et al. (2021). NanoMagSat, a 16U nanosatellite constellation high-precision magnetic project to monitor the Earth's magnetic field and ionospheric environment. In *Egu general assembly abstracts* (Vol. 2021). https://doi.org/10.5194/egusphere-egu21-14660

Jiang, Y., Finlay, C. C., Olsen, N., Tøffner-Clausen, L., Yan, Q., & Zhang, K. (2024). Macau scientific Satellite-1 initial magnetic field model. *Geophysical Research Letters*, *51*(22), e2024GL112305. https://doi.org/10.1029/2024gl112305

Kelbert, A. (2020). The role of global/regional earth conductivity models in natural geomagnetic hazard mitigation. *Surveys in Geophysics*, *41*(1), 115–166. https://doi.org/10.1007/s10712-019-09579-z

Kloss, C., Finlay, C. C., Olsen, N., Tøffner-Clausen, L., Gillet, N., & Grayver, A. (2025). CHAOS-8 geomagnetic field model [Software]. *Zenodo*. https://doi.org/10.5281/zenodo.15806240

Kruglyakov, M., Kuvshinov, A., & Nair, M. (2022). A proper use of the adjacent land-based observatory magnetic field data to account for the geomagnetic disturbances during offshore directional drilling. *Space Weather*, *20*(12), e2022SW003238. https://doi.org/10.1029/2022SW003238

Kuvshinov, A. (2008). 3-D global induction in the oceans and solid Earth: Recent progress in modeling magnetic and electric fields from sources of magnetospheric, ionospheric and oceanic origin. *Surveys in Geophysics*, *29*(2), 139–186. https://doi.org/10.1007/s10712-008-9045-z

Laundal, K. M., Skeidsvoll, A. S., Popescu Braileanu, B., Hatch, S. M., Olsen, N., & Vanhamäki, H. (2025). Global inductive magnetosphere-ionosphere-thermosphere coupling. *EGUsphere*, *2025*, 1–48. Retrieved from https://egusphere.copernicus.org/preprints/2025/egusphere-2025-2051/doi:10.5194/egusphere-2025-2051

Lawrence, E., Beggan, C. D., Richardson, G. S., Reay, S., Thompson, V., Clarke, E., et al. (2025). The geomagnetic and geoelectric response to the May 2024 geomagnetic storm in the United Kingdom. *Frontiers in Astronomy and Space Sciences*, *12*, 1550923. https://doi.org/10.3389/fspas.2025.1550923

Lazzús, J., & Salfate, I. (2024). Report on the effects of the May 2024 Mother's day geomagnetic storm observed from Chile. *Journal of Atmospheric and Solar-Terrestrial Physics*, *261*, 106304. https://doi.org/10.1016/j.jastp.2024.106304

Lee, W., Liu, G., Wu, D. L., & Rowland, D. E. (2025). Ionospheric response to the 10 May 2024 geomagnetic storm as observed in GNSS radio occultation electron density. *Journal of Geophysical Research: Space Physics*, *130*(3), e2024JA033489. https://doi.org/10.1029/2024ja033489

Macmillan, S., & Olsen, N. (2013). Observatory data and the Swarm mission. *Earth Planets and Space*, *65*(11), 1355–1362. https://doi.org/10.5047/eps.2013.07.011

Maus, S., & Lühr, H. (2005). Signature of the quiet-time magnetospheric magnetic field and its electromagnetic induction in the rotating Earth. *Geophysical Journal International*, *162*(3), 755–763. https://doi.org/10.1111/j.1365-246x.2005.02691.x

Maute, A., & Richmond, A. D. (2016). F-region dynamo simulations at low and mid-latitude. *Space Science Reviews*, *206*(1–4), 471–493. https://doi.org/10.1007/s11214-016-0262-3

Min, J., & Grayver, A. (2025). A decade of the fast-varying ionospheric and magnetospheric magnetic fields. *Geophysical Journal International*, *241*(2), 797–825. https://doi.org/10.1093/gji/ggaf065

Nayak, C., Buchert, S., Yiğit, E., Ankita, M., Singh, S., Tulasi Ram, S., & Dimri, A. (2025). Topside low-latitude ionospheric response to the 10–11 May 2024 super geomagnetic storm as observed by swarm: The strongest storm-time super-fountain during the swarm era? *Journal of Geophysical Research: Space Physics*, *130*(3), e2024JA033340. https://doi.org/10.1029/2024ja033340

Olsen, N. (1997). Ionospheric F region currents at middle and low latitudes estimated from MAGSAT data. *Journal of Geophysical Research*, *102*(A3), 4563–4576. https://doi.org/10.1029/96JA02949

Olsen, N., Albini, G., Bouffard, J., Parrinello, T., & Tøffner-Clausen, L. (2020). Magnetic observations from CRYOSAT-2: Calibration and processing of satellite platform magnetometer data. *Earth Planets and Space*, *72*, 1–18. https://doi.org/10.1186/s40623-020-01171-9

Olsen, N., & Floberghagen, R. (2018). Exploring geospace from space: The swarm satellite constellation mission. *Space Research Today*, *203*, 61–71. https://doi.org/10.1016/j.srt.2018.11.017

Olsen, N., Friis-Christensen, E., Floberghagen, R., Alken, P., Beggan, C. D., Chulliat, A., et al. (2013). The Swarm satellite constellation application and research facility (SCARF) and Swarm data products. *Earth Planets and Space*, *65*(11), 1189–1200. https://doi.org/10.5047/eps.2013.07.001

Olsen, N., & Kuvshinov, A. (2004). Modeling the ocean effect of geomagnetic storms. *Earth Planets and Space*, *56*(5), 525–530. https://doi.org/10.1186/bf03352512

Owen, A. B. (2007). A robust hybrid of lasso and ridge regression. *Contemporary Mathematics*, *443*(7), 59–72. https://doi.org/10.1090/conm/443/08555

Parker, W. E., & Linares, R. (2024). Satellite drag analysis during the May 2024 Gannon geomagnetic storm. *Journal of Spacecraft and Rockets*, *61*(5), 1412–1416. https://doi.org/10.2514/1.a36164

Pedregosa, F., Varoquaux, G., Gramfort, A., Michel, V., Thirion, B., Grisel, O., et al. (2011). Scikit-learn: Machine learning in Python. *Journal of Machine Learning Research*, *12*, 2825–2830. https://doi.org/10.5555/1953048.2078195

Roelof, E. C., & Williams, D. J. (1988). The terrestrial ring current: From in situ measurements to global images using energetic neutral atoms. *Johns Hopkins APL Technical Digest*, *9*, 144–163.

Sabaka, T. J., Hulot, G., & Olsen, N. (2010). Mathematical properties relevant to geomagnetic field modeling. In *Handbook of geomathematics*. https://doi.org/10.1007/978-3-642-01546-5_17

Sabaka, T. J., Olsen, N., & Langel, R. A. (2002). A comprehensive model of the quiet-time, near-Earth magnetic field: Phase 3. *Geophysical Journal International*, *151*(1), 32–68. https://doi.org/10.1046/j.1365-246x.2002.01774.x

Sabaka, T. J., Tøffner-Clausen, L., Olsen, N., & Finlay, C. C. (2020). CM6: A comprehensive geomagnetic field model derived from both CHAMP and Swarm satellite observations. *Earth Planets and Space*, *72*(1), 1–24. https://doi.org/10.1186/s40623-020-01210-5

Schmucker, U. (1985). Sources of the geomagnetic field. In *Landolt-börnstein, new-series, 5/2b* (pp. 31–73). Springer-Verlag.

Smith, A., Pačes, M., & Santillan, D. (2025). ESA-VirES/VirES-Python-Client [Software]. *Zenodo*. https://doi.org/10.5281/zenodo.15292625

Smith, J., Kast, A., Geraschenko, A., Morton, Y. J., Brenner, M. P., van Diggelen, F., & Williams, B. P. (2024). Mapping the ionosphere with millions of phones. *Nature*, *635*(8038), 365–369. https://doi.org/10.1038/s41586-024-08072-x

Spogli, L., Alberti, T., Bagiacchi, P., Cafarella, L., Cesaroni, C., Cianchini, G., et al. (2024). The effects of the May 2024 Mother's day superstorm over the Mediterranean sector: From data to public communication. *Annals of Geophysics*, *67*(2), PA218. https://doi.org/10.4401/ag-9117

Stolle, C., Michaelis, I., Xiong, C., Rother, M., Usbeck, T., Yamazaki, Y., et al. (2021). Observing Earth's magnetic environment with the GRACE-FO mission. *Earth Planets and Space*, *73*, 1–21. https://doi.org/10.1186/s40623-021-01364-w

Tulasi Ram, S., Veenadhari, B., Dimri, A., Bulusu, J., Bagiya, M., Gurubaran, S., et al. (2024). Super-intense geomagnetic storm on 10–11 May 2024: Possible mechanisms and impacts. *Space Weather*, *22*(12), e2024SW004126. https://doi.org/10.1029/2024sw004126

Wang, H., Lühr, H., Ma, S. Y., Weygand, J., Skoug, R. M., & Yin, F. (2006). Field-aligned currents observed by CHAMP during the intense 2003 geomagnetic storm events. *Annales Geophysicae*, *24*(1), 311–324. https://doi.org/10.5194/angeo-24-311-2006

Yamazaki, Y. (2022). Solar and lunar daily geomagnetic variations and their equivalent current systems observed by Swarm. *Earth Planets and Space*, *74*(1), 99. https://doi.org/10.1186/s40623-022-01656-9

Yamazaki, Y., & Maute, A. (2017). Sq and EEJ—A review on the daily variation of the geomagnetic field caused by ionospheric dynamo currents. *Space Science Reviews*, *206*(1–4), 299–405. https://doi.org/10.1007/978-94-024-1225-3_12

Zenhäusern, G., Kuvshinov, A., Guzavina, M., & Maute, A. (2021). Towards probing Earth's upper mantle with daily magnetic field variations: Exploring a physics-based parametrization of the source. *Earth Planets and Space*, *73*(1), 1–16. https://doi.org/10.1186/s40623-021-01455-8

Zhang, K. (2023). A novel geomagnetic satellite constellation: Science and applications. *Earth and Planetary Physics*, *7*(1), 4–21. https://doi.org/10.26464/epp2023019

Zhang, K. (2025). Macau scientific satellite 1 vector field magnetometer (VFM) [Dataset]. *Macao Institute of Space Science and Technology*. Retrieved from https://mss.must.edu.mo/data.html

Zhang, Z., Zhang, F., Wang, L., Li, X., Zhima, Z., Wang, Y., et al. (2025). The magnetosphere-ionosphere-ground responses to the May 2024 super solar storm. *Space Weather*, *23*(4), e2024SW004197. https://doi.org/10.1029/2024SW004197